Large anomalous Nernst effect and topological Nernst effect in the noncollinear antiferromagnet $NdMn_2Ge_2$

Chunqiang Xu,[1,2,*] Wei Tian,[3] Pengpeng Zhang,[1] and Xianglin Ke[1,†]

[1]*Department of Physics and Astronomy, Michigan State University, East Lansing, Michigan 48824-2320, USA*
[2]*School of Physical Science and Technology, Ningbo University, Ningbo 315211, China*
[3]*Neutron Scattering Division, Oak Ridge National Laboratory, Oak Ridge, Tennessee 37831, USA*

(Received 24 May 2023; accepted 16 August 2023; published 25 August 2023)

$ThCr_2Si_2$-type $NdMn_2Ge_2$ was recently proposed to be a magnetic skyrmion candidate exhibiting the topological Hall effect. In this work, we report magnetic, electronic, and thermoelectric measurements for $NdMn_2Ge_2$ single crystals. We show that, in the canted antiferromagnetic phase and the conical magnetic phase with a large out-of-plane ferromagnetic component, this system exhibits both an anomalous Nernst effect and a topological Nernst effect. We argue that $NdMn_2Ge_2$ is a unique magnetic material, with its topological characteristics associated with the Berry phases in both real space and momentum space.

DOI: 10.1103/PhysRevB.108.064430

I. INTRODUCTION

In nonmagnetic metals, in the presence of a longitudinal electric field and a perpendicular magnetic field, a transverse voltage is induced due to the Lorentz force, which is known as the normal Hall effect. In ferromagnetic metallic systems, an additional transverse voltage emerges, termed the anomalous Hall effect (AHE), which is fundamentally driven by the spin-orbit interaction. The anomalous Hall resistivity is often proportional to spontaneous magnetization instead of an external magnetic field [1,2]. Recently, a third contribution to the Hall effect, coined the topological Hall effect (THE), was proposed in some magnetic systems with noncoplanar spin configurations [3–7]. Owing to the noncoplanar spin structure, the resultant nonzero spin chirality $\chi = S_i \bullet (S_j \times S_k)$, where S_i, S_j, and S_k are the three nearest-neighboring spins, induces a nontrivial Berry phase and an associated fictitious magnetic field that gives rise to the THE [8–12]. The THE has been detected in magnetic skyrmion systems that host swirling vortex-like spin textures.

As the counterpart of electronic transport measurements, thermoelectric transport measurements are effective probes to study thermoelectric properties of magnetic materials [12–17]. For instance, the anomalous Nernst effect (ANE), a transverse voltage generated in the presence of a longitudinal temperature gradient, is found to be associated with the Berry curvature of electronic bands near the Fermi level and thus has been recently applied in studying topological electronic materials [18,19]. From the technological viewpoint, materials showing an appreciable Nernst effect are promising candidates for both thermoelectric and spintronic applications [20,21]. In comparison to the electric Hall effect, both the ANE and the topological Nernst effect (TNE) have been much less studied due to the lack of suitable candidate materials.

Very recently, it was reported that $NdMn_2Ge_2$, a centrosymmetric compound with a $ThCr_2Si_2$-type structure, exhibits a large THE with a maximum value of ~ 2.05 μΩ cm over a wide range of magnetic fields and temperatures [22,23]. And a Lorentz transmission electron microscopy (LTEM) study [22] revealed the existence of magnetic skyrmions in this compound. Therefore, $NdMn_2Ge_2$ is a great candidate material for studying its thermoelectric properties. In this work, we report comprehensive magnetic, electronic, and thermoelectric transport measurements of $NdMn_2Ge_2$ single crystals. We show that $NdMn_2Ge_2$ exhibits both an ANE with $|S^A_{xy}| \sim 1.4$ μV K^{-1} and a TNE with $|S^T_{xy}| \sim 0.3$ μV K^{-1}. The anomalous thermoelectric linear response tensor $|\alpha^A_{xy}|$ reaches ~ 0.6 A m^{-1} K^{-1}, and $|S^T_{xy}|$ is found to be comparable to values reported previously in other topological systems.

II. METHODS

$NdMn_2Ge_2$ single crystals were grown using the indium flux method. The high-purity elements neodymium, manganese, germanium, and indium as starting materials were mixed with a molar ratio of 1:2:2:30 and were sealed in a vacuum quartz tube. The quartz tube was loaded into a box-type furnace that was heated to 1100°C and kept at this temperature for 10 h for the raw materials to be thoroughly melted. Then the furnace was slowly cooled down to 700°C at a rate of 3°C/h before taking out the quartz tube for centrifuging. Afterward, the as-grown shiny, plate-like single crystals with a typical size of 3×2×0.2 mm were obtained. Magnetic susceptibility was measured using a Quantum Design SQUID magnetometer (MPMS3), and the electronic transport measurements were carried out using a Quantum Design cryostat (PPMS). Single-crystal neutron diffraction measurements were performed using the HB1A triple-axis spectrometer in

*Corresponding author: xuchunqiang@nbu.edu.cn
†ke@pa.msu.edu

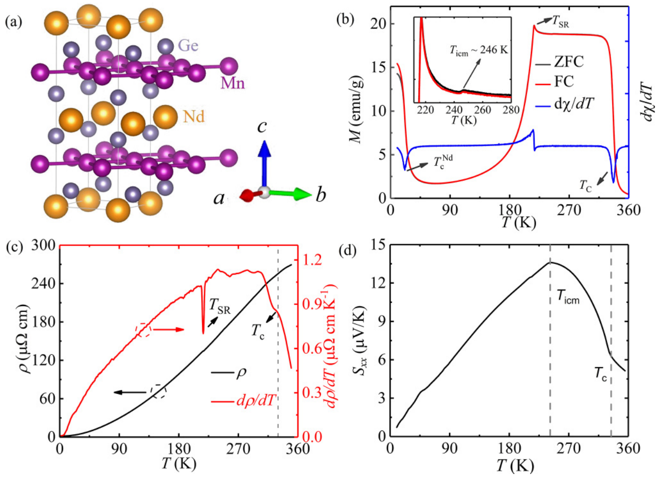

FIG. 1. (a) The schematic crystal structure of $NdMn_2Ge_2$. (b) Temperature dependence of the magnetic moment measured under FC and ZFC conditions with an applied magnetic field of 0.1 T. Inset shows an expanded view near T_{icm}. (c) Temperature dependence of longitudinal resistivity ρ_{xx} (left axis) and it is derivative $\frac{d\rho_{xx}}{dT}$ (right axis). (d) Temperature dependence of the Seebeck coefficient S_{xx}.

the High Flux Isotope Reactor at Oak Ridge National Laboratory. The energy of incident neutrons was fixed as 14.6 meV. A single crystal sample was oriented in the $(H\ 0\ L)$ and $(H\ K\ 0)$ planes, where H, K, and L are in reciprocal lattice units. The sample was mounted inside a closed-cycle helium refrigerator with a measurement temperature range of 5 to 300 K. Thermoelectric measurements were carried out using a modified sample puck designed to be compatible with the PPMS cryostat. The temperature was probed using type-E (Constantan-Chromel) thermocouples, and the thermoelectric voltage was measured using a Keithley Instruments K2182A nanovoltmeter. For all measurements presented in this work, the magnetic field was applied along the c-axis.

III. RESULTS

The $NdMn_2Ge_2$ compound crystallizes in the tetragonal space group $I4/mmm$ (No. 139) with lattice parameters $a = b = 4.110$ Å and $c = 10.845$ Å. Figure 1(a) illustrates the schematic crystal structure of $NdMn_2Ge_2$. The neighboring manganese (and neodymium) atoms form square lattices in the ab plane with the neighboring manganese (neodymium) layers separated from each other by $c/2$. Previous neutron powder diffraction measurements revealed that this system undergoes multiple magnetic phase transitions upon cooling: a paramagnetic-to-antiferromagnetic transition occurs at $\sim$480 K, below which manganese spins form a collinear antiferromagnetic spin structure; below $\sim$330 K, the magnetic structure changes to a canted antiferromagnetic structure with a net ferromagnetic component of manganese spins aligned along the c-axis, which is subsequently followed by another magnetic transition to a conical spin structure below $\sim$250 K. Finally a ferromagnetic ordering of the neodymium sublattice at $\sim$100 K was reported [22,24].

In Fig. 1(b), we plot the temperature dependence of magnetic susceptibility $\chi(T)$ measured with a magnetic field

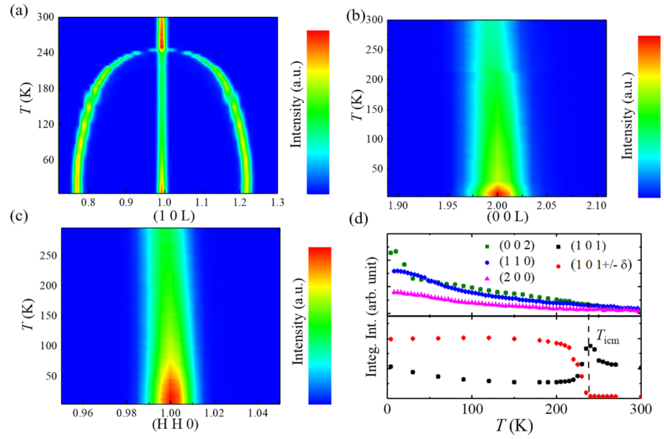

FIG. 2. (a)–(c) False-color contour maps of T–[1 0 L], T–[0 0 L], and T–[H H 0] measured at 0 T. (d) Temperature dependence of integrated neutron scattering intensity of (0 0 2), (1 1 0), (2 0 0), and (1 0 1), and (1 0 1 $\pm$ δ) Bragg reflections.

of 0.1 T applied along the c-axis under zero-field cooling (ZFC) and field-cooling (FC) conditions. As clearly seen from the $d\chi/dT$ (blue) curve, within the measurement temperature range, $NdMn_2Ge_2$ exhibits three magnetic phase transitions at $T_c \sim 337$ K, $T_{SR} \sim 216$ K, and $T_{Nd} \sim 21.5$ K, corresponding to the collinear-to-canted antiferromagnetic transition of manganese spins, the spin reorientation of manganese spins, and the ferromagnetic ordering of neodymium spins, respectively. These features are consistent with a recent report [23]. Additionally, another anomaly at $T_{icm} \sim 246$ K is also visible, as seen in the expanded view of $\chi(T)$ shown in the inset, which corresponds to the transition to an incommensurate conical spin structure (which is discussed later).

Figure 1(c) shows the temperature dependence of in-plane resistivity ρ_{xx} and its derivative $\frac{d\rho_{xx}}{dT}$ measured at zero field. The residual resistivity ratio reaches a value of $\sim$160, indicating the high quality of the as-grown single crystals. Notably, while ρ_{xx} monotonically increases with increasing temperature, an anomaly is clearly seen in $\frac{d\rho_{xx}}{dT}$ at T_{SR}. In addition, a kink in $\frac{d\rho_{xx}}{dT}$ near the canted antiferromagnetic phase transition T_c is also observed (see the dashed line). In Fig. 1(d), we present the temperature-dependent Seebeck coefficient S_{xx} with a thermal gradient applied in the ab plane. The positive S_{xx} value over the whole measurement temperature range indicates that the p-type (hole) charge carriers dominate in $NdMn_2Ge_2$. S_{xx} shows a broad peak with a value of 13.6 μV K^{-1} around T_{icm} and a kink near T_c. These features suggest that both electronic and thermoelectric transport properties of $NdMn_2Ge_2$ are closely correlated with the complex magnetic configurations of this system.

To revisit the magnetic structure of $NdMn_2Ge_2$, we performed single-crystal neutron diffraction measurements. Figures 2(a)–2(c) shows false-color contour maps of T–[1 0 L], T–[0 0 L], and T–[H H 0] measured at 0 T. Two features are clearly seen. First, a commensurate-to-incommensurate phase transition occurs at T_{icm}, with incommensurate magnetic Bragg peaks of (1 0 1 $\pm$ δ), where δ

increases with decreasing temperature and then nearly saturates with a value of 0.217(1) at low temperature. Second, the neutron diffraction intensity of nuclear Bragg reflections also varies with temperature, indicating the contribution from the magnetic moment that superimposes with the nuclear Bragg peak intensity. Figure 2(d) shows the temperature dependence of an integrated neutron scattering intensity of (0 0 2), (1 1 0), (2 0 0), and (1 0 1), and (1 0 1 $\pm$ δ) Bragg reflections. Note that a ferromagnetic component of manganese spins gives rise to an enhanced diffraction intensity of Bragg reflections with $H + K = \text{even}$, while an antiferromagnetic ordering of manganese spins yields an enhancement in the diffraction intensity of Bragg reflections with $H + K = \text{odd}$ [24]. Since neutrons couple to the magnetic moment perpendicular to the moment transfer **q**, the observed monotonic increase in the diffraction intensities of (0 0 2), (1 1 0), and (2 0 0) over the whole measurement temperature range suggests that the net ferromagnetic moment of manganese spins in both the canted antiferromagnetic state ($T_{\text{icm}} < T < T_{\text{c}}$) and the conical spin state for $T_{\text{SR}} < T < T_{\text{icm}}$ and $T < T_{\text{SR}}$ is not strictly aligned either along the c-axis or in the ab plane. This is distinct from a previous neutron power diffraction study [24] that concluded that the net ferromagnetic moment of manganese is along the c-axis for $T_{\text{SR}} < T < T_{\text{c}}$ and in the ab plane for $T < T_{\text{SR}}$, while indeed the net ferromagnetic component of manganese tends to tilt from the c-axis toward the ab place when cooling across T_{SR}, as seen from the magnetic susceptibility data shown in Fig. 1(b) (also see Ref. [23]). The sharp increase in the (0 0 2) Bragg intensity below 25 K, which is absent in both (2 0 0) and (1 1 0) Bragg reflections, arises from the long-range ordering of neodymium spins aligned in the ab plane. In addition, the commensurate-to-incommensurate phase transition below T_{icm} is clearly indicated by the decrease/increase of the diffraction intensity of (1 0 1)/(1 0 1 $\pm$ δ) Bragg peaks. The schematic sketches of magnetic structures are presented in Supplemental Material Fig. S1 [25].

We now turn to a discussion of thermoelectric measurement results. Figure 3(a) shows the magnetic field dependence of the Nernst coefficient $-S_{xy}$ measured at various temperatures. A thermal gradient is applied along the longitudinal direction (x-axis) and the magnetic field is applied along the perpendicular direction [$c(z)$-axis], and the voltage is measured along the transverse direction (y-axis). One can see that above 220 K, $-S_{xy}$ increases rapidly at low fields and then saturates, while the saturation field gradually increases at lower temperatures. The latter feature is associated with the spin reorientation transition at $\sim T_{\text{SR}}$, with the net ferromagnetic moment tilting from near the c-axis toward near the ab plane, consistent with the $M(H)$ data shown in Supplemental Material Fig. S2 [25]. There is no visible hysteresis loop in both the $-S_{xy}$ and $M(H)$ curves, implying that domain walls propagate smoothly without flux pinning in $NdMn_2Ge_2$ during the field-sweeping process. Like the field-dependent ρ_{yx} (Supplemental Material Fig. S3(a) [25]), the saturated $-S_{xy}$ at high fields suggests the nature of the ANE. As discussed previously, recent electronic transport measurements revealed that, in addition to the normal Hall effect and an AHE contribution, the third contribution, THE, which stems from the finite scalar spin chirality associated with the noncoplanar spin configuration that gives rise to nonzero real-space Berry

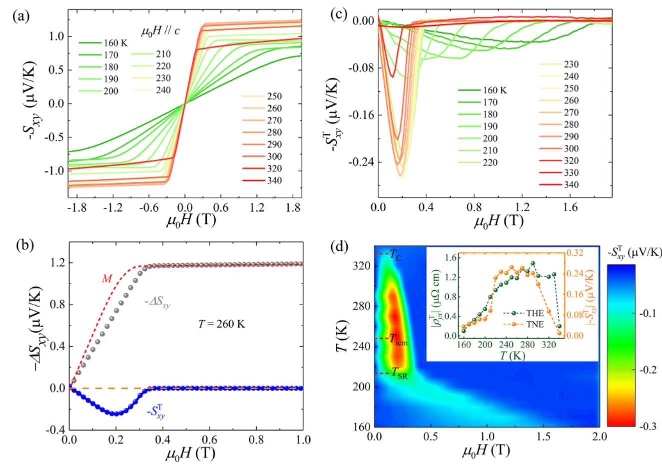

FIG. 3. (a) Magnetic field dependence of Nernst thermopower $-S_{xy}$ measured at various temperatures. (b) Magnetic field dependence of magnetic moment M, $-\Delta S_{xy}$, and the extracted topological Nernst $-S^T_{xy}$ at 260 K. (c) Magnetic field dependence of $-S^T_{xy}$ measured at different temperatures. Each curve is obtained using the method as described in (b). (d) The T-H contour map of $-S^T_{xy}$. The transition temperatures are denoted with dashed red lines. The inset is the temperature dependence of the maximum values of $|\rho^T_{yx}|$ (left axis) and $|-S^T_{xy}|$ (right axis).

curvature, emerges [23]. As a result, one anticipates observing the TNE contribution to the total Nernst effect. That is, $S_{xy} = S_0 + S^A_{xy} + S^T_{xy}$, where S_0, S^A_{xy}, and S^T_{xy} represent the normal ($\sim H$), anomalous ($\sim M$), and topological contributions to the Nernst effect, respectively.

To extract the topological contribution to the observed Nernst signal, S^T_{xy}, we overplot the $-\Delta S_{xy}(H)$ and the magnetization data $M(H)$ for each temperature measured. $\Delta S_{xy}(H)$ is obtained after subtracting the S_0 term from the measured S_{xy} by performing linear fitting using the high field data. For instance, we present such data measured at $T = 260$ K in Fig. 3(b). It is clearly seen that the magnetic field dependence of ΔS_{xy} and M do not overlap exactly in the low field region, suggesting a topological contribution to the observed Nernst effect. By assuming that S^A_{xy} is proportional to M, we can further subtract the S^A_{xy} term from ΔS_{xy} to obtain the TNE contribution S^T_{xy}. The thus-extracted $-S^T_{xy}$ at 260 K is represented by the blue curve in Fig. 3(b), which shows a broad peak with a maximum value of approximately -0.26 μV K^{-1} at the low field. $-S^T_{xy}$ approaches zero when H is close to the saturation field. These features are similar to those found in Fe_3Sn_2, which hosts magnetic skyrmions [26].

In Fig. 3(c), we present the field dependence of $-S^T_{xy}$ at various temperatures, and a T-H contour map of $-S^T_{xy}$ is shown in Fig. 3(d). It is obviously seen that $-S^T_{xy}$ reaches high values within a narrow T-H region, a feature similar to what is found in the THE (ρ^T_{yx}) data shown in Supplemental Material Fig. S3(b)–S3(d) [25]. The temperature dependence of the maximum $|-S^T_{xy}|$ measured at each temperature is shown in the inset of Fig. 3(d). For comparison, we also plot the temperature dependence of the maximum $|\rho^T_{yx}|$. Overall, the shapes of $|-S^T_{xy}|$ and $|\rho^T_{yx}|$ are similar, showing nonmonotonic temperature dependence. Both curves exhibit a plateau-like

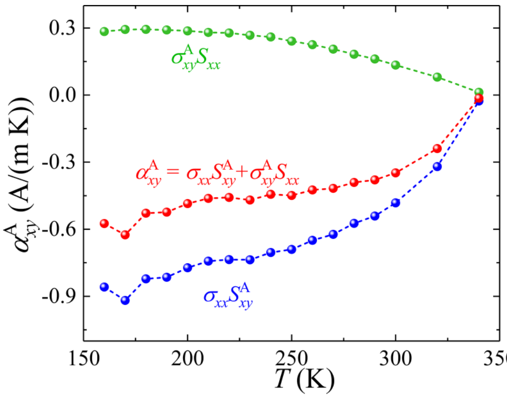

FIG. 4. Temperature dependence of the total anomalous transverse thermoelectric conductivity α^A_{xy} and its two components $\sigma_{xx}S^A_{xy}$ and $\sigma^A_{xy}S_{xx}$.

feature with large TNE and THE between 220 K to 320 K, implying that the TNE and THE behaviors are of a common physical origin. Recent LTEM studies revealed the existence of skyrmion bubbles; however, the skyrmion bubbles persist in a wide temperature range from 330 K down to 150 K (at which both the TNE and THE signal are quite small) and do not show noticeable magnetic field dependence [22]. This suggests that the TNE and THE behaviors are not mainly driven by the nonzero spin chirality associated with skyrmion bubbles. Instead, a plausible mechanism can be ascribed to the noncoplanar spin structure with a large out-of-plane ferromagnetic component in $NdMn_2Ge_2$. As discussed previously, between T_{SR} and T_{icm}, $NdMn_2Ge_2$ exhibits a conical spin structure, while between T_{icm} and T_c it exhibits a canted antiferromagnetic spin structure in the absence of a magnetic field with a net ferromagnetic moment having components both in the *ab* plane and along the *c*-axis. This suggests a delicate energetic competition between the canted antiferromagnetic phase and the incommensurate conical phase. As a result, an applied magnetic field along the *c*-axis may tip the energetic balance and give rise to the noncoplanar spin structure between T_{icm} and T_c, which accounts for the nonvanishing THE and TNE observed. It is desirable to probe the field-induced spin structure using neutron diffraction measurements.

To quantify the ANE in $NdMn_2Ge_2$ further, we calculate the anomalous transverse thermoelectric conductivity α^A_{xy}. Using the measured components of σ_{xx}, σ^A_{xy}, S_{xx}, and S^A_{xy}, we determine α^A_{xy} in terms of $\alpha^A_{xy} = \sigma_{xx}S^A_{xy} + \sigma^A_{xy}S_{xx}$ [27,28], where σ_{xx} and σ^A_{xy} are calculated as $\sigma_{xx} = \frac{\rho_{xx}}{\rho^2_{xx}+\rho^2_{yx}}$ and $\sigma^A_{xy} = \frac{\rho^A_{yx}}{\rho^2_{xx}+\rho^2_{yx}}$, respectively. Note that these transverse thermoelectric and electronic conductivity tensors are directly associated with the Berry curvature Ω^Z, with σ^A_{xy} being proportional to the integration of Ω^Z of the whole Fermi sea, while α^A_{xy} is proportional to the integrated Ω^Z in the momentum space near the Fermi surface [18,29]. Figure 4 presents the temperature dependence of $\sigma^A_{xy}S_{xx}$, $\sigma_{xx}S^A_{xy}$, and α^A_{xy} extracted at 1.8 T, the magnitude of which all increase with decreasing temperature within the measurement temperature range. Note that the first two terms have an opposite sign, and such a feature is similar to that observed in other topological semimetals, such as Mn_3Ge [18] and Fe_3Sn_2 [26]. The maximum value (at $T = 160$ K) of $|\alpha^A_{xy}|$ reaches ~ 0.6 A m^{-1}K^{-1}, which is comparable with results reported in Mn_3Ge and Fe_3Sn_2 with $\alpha^A_{xy} \sim 1.0$ A m^{-1}K^{-1} [18,26]. By simply fitting ρ_{xy} to ρ_{xx} (i.e., $\rho_{xy} \sim \rho_{xx}$), it was previously argued that the AHE between 150 K and 250 K is driven by skew scattering of the charge carriers [23]. Note that skew scattering tends to be the dominant factor in highly conductive metals whose resistivity is smaller than 1 $\mu\Omega$ cm [29]. However, as shown in Fig. 1(c) (also see Ref. [23]), within this temperature range the resistivity of $NdMn_2Ge_2$ is 100 to 200 $\mu\Omega$ cm, suggesting that $NdMn_2Ge_2$ is not a highly conductive metal, which implies that skew scattering is not dominant. Furthermore, instead of linearly fitting ρ_{yx} to ρ_{xx} between 150 K and 250 K, as shown in Supplemental Material Fig. S4 [25], we find that our own ρ_{yx}/M (instead of just ρ_{yx}) data can be nicely fitted with both linear and quadratic terms of ρ_{xx} between 160 K and 320 K, i.e., $\rho_{xy} \sim a(M)\rho_{xx} + b(M)\rho^2_{xx}$, assuming that both $a(M)$ and $b(M)$ terms are proportional to M [29]. This suggests the contributions from skew scattering and intrinsic contributions associated with the electronic structure to the AHE. The *ab initio* calculations of electronic band structure are desirable to understand further the origin of the anomalous Hall and anomalous thermoelectric conductivity in this system.

IV. CONCLUSION

In summary, we synthesized $NdMn_2Ge_2$ single crystals and performed neutron diffraction, and electronic and thermoelectric transport studies. We show that $NdMn_2Ge_2$ exhibits a large topological Nernst effect and an anomalous Nernst effect, with the former feature driven by the noncoplanar spin structure and the latter feature related to the combined effects of skew scattering and Berry curvature of electronic bands. These results suggest $NdMn_2Ge_2$ is a rare candidate that possesses topological properties associated with Berry phases in both real space and momentum space.

ACKNOWLEDGMENTS

X.K. acknowledges the financial support provided by the U.S. Department of Energy (DOE), Office of Science, Office of Basic Energy Sciences, Materials Sciences and Engineering Division (Grant No. DE-SC0019259). P.Z. acknowledges the financial support provided by the National Science Foundation (Grant No. DMR-2112691). C.X. is partially supported by the startup funds at Michigan State University. A portion of this research used resources at the High Flux Isotope Reactor, the DOE Office of Science User Facility, operated by the Oak Ridge National Laboratory.

[1] E. H. Hall, On a new action of the magnet on electric currents, Am. J. Math. **2**, 287 (1879).

[2] E. H. Hall, XVIII, On the “Rotational Coefficient” in nickel and cobalt, Philos. Mag. **12**, 157 (1881).

[3] Y. O. Y. Taguchi, H. Yoshizawa, N. Nagaosa, and Y. Tokura, Spin chirality, Berry phase, and anomalous Hall effect in a frustrated ferromagnet, Science **291**, 2573 (2001).

[4] Y. Machida, S. Nakatsuji, Y. Maeno, T. Tayama, T. Sakakibara, and S. Onoda, Unconventional Anomalous Hall Effect Enhanced by a Noncoplanar Spin Texture in the Frustrated Kondo Lattice $Pr_2Ir_2O_7$, Phys. Rev. Lett. **98**, 057203 (2007).

[5] H. Takatsu, S. Yonezawa, S. Fujimoto, and Y. Maeno, Unconventional Anomalous Hall Effect in the Metallic Triangular-Lattice Magnet $PdCrO_2$, Phys. Rev. Lett. **105**, 137201 (2010).

[6] Q. Wang, Q. Yin, and H. Lei, Giant topological Hall effect of ferromagnetic kagome metal Fe_3Sn_2, Chin. Phys. B **29**, 017101 (2020).

[7] G. Gong, L. Xu, Y. Bai, Y. Wang, S. Yuan, Y. Liu, and Z. Tian, Large topological Hall effect near room temperature in noncollinear ferromagnet $LaMn_2Ge_2$ single crystal, Phys. Rev. Mater. **5**, 034405 (2021).

[8] J. Ye, Y. B. Kim, A. J. Millis, B. I. Shraiman, P. Majumdar, and Z. Tesanovic, Berry Phase Theory of the Anomalous Hall Effect: Application to Colossal Magnetoresistance Manganites, Phys. Rev. Lett. **83**, 3737 (1999).

[9] P. Bruno, V. K. Dugaev, and M. Taillefumier, Topological Hall Effect and Berry Phase in Magnetic Nanostructures, Phys. Rev. Lett. **93**, 096806 (2004).

[10] F. Caglieris, C. Wuttke, S. Sykora, V. Süss, C. Shekhar, C. Felser, B. Büchner, and C. Hess, Anomalous Nernst effect and field-induced Lifshitz transition in the Weyl semimetals TaP and TaAs, Phys. Rev. B **98**, 201107(R) (2018).

[11] X. Li, L. Xu, L. Ding, J. Wang, M. Shen, X. Lu, Z. Zhu, and K. Behnia, Anomalous Nernst and Righi-Leduc Effects in Mn_3Sn: Berry Curvature and Entropy Flow, Phys. Rev. Lett. **119**, 056601 (2017).

[12] J. Xu, W. A. Phelan, and C. L. Chien, Large anomalous Nernst effect in a van der Waals ferromagnet Fe_3GeTe_2, Nano. Lett. **19**, 8250 (2019).

[13] Y. Shiomi, N. Kanazawa, K. Shibata, Y. Onose, and Y. Tokura, Topological Nernst effect in a three-dimensional skyrmion-lattice phase, Phys. Rev. B **88**, 064409 (2013).

[14] M. Ikhlas, T. Tomita, T. Koretsune, M.- T. Suzuki, D. Nishio-Hamane, R. Arita, Y. Otani, and S. Nakatsuji, Large anomalous Nernst effect at room temperature in a chiral antiferromagnet, Nat. Phys. **13**, 1085 (2017).

[15] A. Sakai, Y. P. Mizuta, A. A. Nugroho, R. Sihombing, T. Koretsune, M.- T. Suzuki, N. Takemori, R. Ishii, D. Nishio-Hamane, R. Arita, P. Goswami, and S. Nakatsuji, Giant anomalous Nernst effect and quantum-critical scaling in a ferromagnetic semimetal, Nat. Phys. **14**, 1119 (2018).

[16] S. N. Guin, P. Vir, Y. Zhang, N. Kumar, S. J. Watzman, C. Fu, E. Liu, K. Manna, W. Schnelle, J. Gooth, C. Shekhar, Y. Sun, and C. Felser, Zero-field Nernst effect in a ferromagnetic kagome-lattice Weyl-semimetal $Co_3Sn_2S_2$, Adv. Mater. **31**, e1806622 (2019).

[17] H. Zhang, J. Koo, C. Xu, M. Sretenovic, B. Yan, and X. Ke, Exchange-biased topological transverse thermoelectric effects in a kagome ferrimagnet, Nat. Commun. **13**, 1091 (2022).

[18] C. Wuttke, F. Caglieris, S. Sykora, F. Scaravaggi, A. U. B. Wolter, K. Manna, V. Süss, C. Shekhar, C. Felser, B. Büchner, and C. Hess, Berry curvature unravelled by the anomalous Nernst effect in Mn_3Ge, Phys. Rev. B **100**, 085111 (2019).

[19] Y. Pan, C. Le, B. He, S. J. Watzman, M. Yao, J. Gooth, J. P. Heremans, Y. Sun, and C. Felser, Giant anomalous Nernst signal in the antiferromagnet $YbMnBi_2$, Nat. Mater. **21**, 203 (2022).

[20] Y. Sakuraba, Potential of thermoelectric power generation using anomalous Nernst effect in magnetic materials, Scr. Mater. **111**, 29 (2016).

[21] M. Mizuguchi and S. Nakatsuji, Energy-harvesting materials based on the anomalous Nernst effect, Sci. Technol. Adv. Mater. **20**, 262 (2019).

[22] S. Wang, Q. Zeng, D. Liu, H. Zhang, L. Ma, G. Xu, Y. Liang, Z. Zhang, H. Wu, R. Che, X. Han, and Q. Huang, Giant topological Hall effect and superstable spontaneous skyrmions below 330 K in a centrosymmetric complex noncollinear ferromagnet $NdMn_2Ge_2$, ACS Appl. Mater. Interfaces **12**, 24125 (2020).

[23] X. Zheng, X. Zhao, J. Qi, X. Luo, S. Ma, C. Chen, H. Zeng, G. Yu, N. Fang, S. U. Rehman, W. Ren, B. Li, and Z. Zhong, Giant topological Hall effect around room temperature in noncollinear ferromagnet $NdMn_2Ge_2$ single crystal, Appl. Phys. Lett. **118**, 072402 (2021).

[24] G. V. R. Welter, E. Ressouche, and B. Malaman, Neutron diffraction study of $CeMn_2Ge_2$, $PrMn_2Ge_2$ and $NdMn_2Ge_2$: Evidence of dominant antiferromagnetic components within the (001) Mn planes in ferromagnetic $ThCr_2Si_2$-type manganese ternary compounds, J. Alloys Compd. **218**, 204 (1995).

[25] See Supplemental Material at http://link.aps.org/supplemental/10.1103/PhysRevB.108.064430 for magnetization and electric Hall effect data.

[26] H. Zhang, C. Q. Xu, and X. Ke, Topological Nernst effect, anomalous Nernst effect, and anomalous thermal Hall effect in the Dirac semimetal Fe_3Sn_2, Phys. Rev. B **103**, L201101 (2021).

[27] L. Ding, J. Koo, L. Xu, X. Li, X. Lu, L. Zhao, Q. Wang, Q. Yin, H. Lei, B. Yan, Z. Zhu, and K. Behnia, Intrinsic Anomalous Nernst Effect Amplified by Disorder in a Half-Metallic Semimetal, Phys. Rev. X **9**, 041061 (2019).

[28] T. Liang, J. Lin, Q. Gibson, T. Gao, M. Hirschberger, M. Liu, R. J. Cava, and N. P. Ong, Anomalous Nernst Effect in the Dirac Semimetal Cd_3As_2, Phys. Rev. Lett. **118**, 136601 (2017).

[29] N. Nagaosa, J. Sinova, S. Onoda, A. H. MacDonald, and N. P. Ong, Anomalous Hall effect, Rev. Mod. Phys. **82**, 1539 (2010).